# Shape of the Posterior Vitreous Chamber in Human Emmetropia and Myopia

Bernard Gilmartin, Manbir Nagra, and Nicola S. Logan

School of Life and Health Sciences, Aston University, Birmingham, United Kingdom

PURPOSE. To compare posterior vitreous chamber shape in myopia to that in emmetropia.

METHODS. Both eyes of 55 adult subjects were studied, 27 with emmetropia (mean spherical error [MSE] $\geq -0.55$; $< +0.75$ D; mean $+0.09 \pm 0.36$ D) and 28 with myopia (MSE $-5.87 \pm 2.31$ D). Cycloplegic refraction was measured with a Shin Nippon autorefractor and anterior chamber depth and axial length with a Zeiss IOLMaster. Posterior vitreous chamber shapes were determined from T2-weighted magnetic resonance imaging (3.0-T) using procedures previously reported by our laboratory. Three-dimensional surface model coordinates were assigned to nasal, temporal, superior, and inferior quadrants and plotted in two dimensions to illustrate the composite shape of respective quadrants posterior to the second nodal point. Spherical analogues of chamber shape were constructed to compare relative sphericity between refractive groups and quadrants.

RESULTS. Differences in shape occurred in the region posterior to points of maximum globe width and were thus in general accord with an equatorial model of myopic expansion. Shape in emmetropia is categorized distinctly as that of an oblate ellipse and in myopia as an oblate ellipse of significantly less degree such that it approximates to a sphere. There was concordance between shape and retinotopic projection of respective quadrants into right, left, superior, and inferior visual fields.

CONCLUSIONS. Prolate ellipse posterior chamber shapes were rarely found in myopia, and we propose that spherical shape in myopia may constitute a biomechanical limitation on further axial elongation. Synchronization of quadrant shapes with retinotopic projection suggests that binocular growth is coordinated by processes that operate beyond the optic chiasm.

Keywords: emmetropia, myopia, MRI, ocular shape, ocular biometry

There is a need to understand why the homeostatic mechanisms regulating normal ocular growth between 6 and 15 years of age should fail and as a consequence produce myopia in a high proportion of children.[1–4] Once developed, myopia is a condition that is likely to extend over at least six decades and during that time will carry a significantly increased risk of ocular pathology even for moderate levels.[1] Studies have demonstrated that both pharmaceutical and optical interventions are able to slow progression of myopia.[5,6]

Current optical strategies, based principally on animal myopia experiments,[7,8] reduce the degree of relative peripheral hyperopia while maintaining clear central vision and have resulted in the application of dual focus spectacle[9] and contact lens devices[10–12] and orthokeratology[13–16] to the management of juvenile-onset myopia. A consensus has yet to emerge on the etiological significance of the peripheral refraction in human myopia,[17–20] but its dependence on eye shape[21] has prompted further evaluation of three-dimensional (3D) structural correlates of myopia and its precursor, emmetropia.[1]

Magnetic resonance imaging (MRI) can provide composite images independent of an eye's optical properties and is therefore ideally suited for studies of ocular structure. Atchison et al.[22,23] presented two comprehensive studies on shape of the eye and shape of the retinal surface in myopia and emmetropia with reference to T1-weighted MRI (i.e., two-dimensional [2D] anatomical representations). The first study[22] measured three linear dimensions (internal length, height, and width) by placement of single 3-mm-thick slices in axial and sagittal planes. Using the same data set, the second study[23] fitted nonrotationally symmetrical ellipsoids to the retinal surface using transverse axial and sagittal images derived from MR images. Substantial variation was found between and within subjects in both studies: for eye shape, neither a global expansion model nor an axial elongation model was sufficient to define the entire myopic population,[22] and for retinal shape, retinas of subjects with myopia generally exhibited an oblate rather than prolate shape, although to a lesser degree than in emmetropia.[23]

In contrast to T1-weighted MRI, T2-weighted MRI is able to illustrate internal eye shape by high-contrast delineation of the vitreous–retina interface. Our laboratory was the first to report on the use of T2-weighted MRI to depict in vivo and in 3D the posterior vitreous chamber of the adult human eye for a range of refractive errors.[24]

Several subsequent studies have used T2-weighted MRI to investigate variations in eye shape in children and adults. Ishii et al.[25] in a study of 105 Japanese children aged 1 month to 19 years used elliptic Fourier descriptors to describe eye shape in emmetropia and myopia and defined an oblate-to-prolate pattern of growth that varied with age. The study used a 1.5-T MRI (head coil) and 1.2- to 3-mm slices for the horizontal meridian only. Lim et al.[26] demonstrated in 67 Chinese children

aged between 6 and 7 years that eye shape is different in myopic and nonmyopic children even at a very young age, with the former exhibiting asymmetric axial globe elongation and the latter global expansion. The study used a 32-channel 3.0-T MRI (head coil) and in-plane resolution was 1 by 1 mm. Three further investigations,[27–29] based in Japan, have been carried out by the same department on eye shape in adult patients with emmetropia and with high myopia (>8 D; axial length > 26.5 mm) and associated ocular pathology. Comprehensive qualitative and quantitative analyses were made of the ocular distortions that occur in the posterior pole in high myopia[27,28] and their association with sclera thickness and contour using a swept-source optical coherence tomography prototype instrument.[29] The range of refractive error used to assign patients to a control group of patients with emmetropia was wide: ±1 D[27,28] and ±3 D.[29] The studies used an 8-channel 1.5-T MRI (head coil) that provided a 1.2-mm slice thickness. A recent paper by Lim et al.[30] compared the degree of oblateness and prolateness in 173 full-term newborn Singaporean children based on measurements of eye length, width, and height. Although oblate eyes were identified, mean values indicated that eyes were generally prolate at birth. The study used an 8-channel 1.5-T MRI (head coil) that provided a 1 by 1 by 1 mm resolution.

There are no studies to date that have used T2-weighted MRI to compare ocular dimensions in adults with emmetropia (as generally defined; i.e., mean spherical error (MSE) $\geq -0.55$; $<+0.75$ D) and myopia without associated manifest ocular pathology. The present study uses an 8-channel 3.0-T (head-coil, 1 by 1 by 1 mm resolution) T2-weighted 3D MRI technique[24] to analyze posterior vitreous chamber dimensions of both eyes in adults with emmetropia and myopia. The 3D data are plotted in two dimensions to signify the composite shape of nasal, temporal, superior, and inferior quadrants. The aim of the study is to make a detailed comparison of the degree to which the posterior vitreous chamber of the human myopic eye differs in shape from the emmetropic eye and to consider whether structural differences are likely to have etiological and clinical significance in terms of the onset, development, and treatment of myopia.

## METHODS

### Subjects

Subjects were recruited from staff and students of Aston University and categorized as those with emmetropia ($N = 27$, MSE $\geq -0.55$; $<+0.75$ D) and myopia ($N = 28$). Only data from subjects with at least 2 D MSE of myopia were included in the data set to ensure ample differentiation in ocular dimensions from subjects with emmetropia. Exclusion criteria were cylindrical corrections greater than 2 D and previous history of ocular surgery, trauma, or pathology, in particular ocular pathology known to be associated with myopia.[1] All subjects were in good general and ocular health and had corrected visual acuities of 0.0 logMAR or better in both eyes. Ethical approval was obtained from Aston University Ethics Committee, and the study adhered to the tenets of the Declaration of Helsinki. Written informed consent was obtained from each subject prior to commencement of the study and after explanation of the nature and possible consequences of the study.

### Ocular Biometry

Data were collected from both right and left eyes. Binocular distance refractive error was measured with an infrared binocular open-view autorefractor (Shin Nippon SRW-5000; Ryusyo Industrial Co. Ltd, Osaka, Japan)[31] following cycloplegia using one drop of tropicamide HCl 1% (Minims; Bausch & Lomb, Kingston-Upon-Thames, UK). Five measurements of refraction were taken from both eyes, averaged, and converted to MSE. Corneal radius, anterior chamber depth (ACD), and axial length were measured (all in millimeters) with the Zeiss IOLMaster (Carl Zeiss Meditec, Inc., Dublin, CA).[32] Three separate measurements of corneal radius were averaged, a single capture shot automatically generated and averaged five measurements of ACD, and five separate measurements of axial length were averaged.

### MR Image Acquisition

MR images were obtained for both right and left eyes using the procedures previously reported by our laboratory.[24] In summary, subjects were scanned using a Siemens Trio 3.0-T whole-body MRI scanner using an 8-channel phased-array head-coil. A T2-weighted scan was used to demarcate fluid-based intraocular structures for each eye and thus provide high-contrast delineation of the vitreous–retina interface. The scan used a HASTE sequence with parameters that provided isotropic voxel dimensions of 1 by 1 by 1 mm. The scan time for each subject was 5 minutes 40 seconds, during which they were asked to fixate steadily, with minimal blinking if possible, a distant fixation light viewed through a mirror mounted on the head-coil. Subjects with myopia were uncorrected but were able to maintain fixation during the scanning period. Voxels were labeled using a 3D flood-filling algorithm and automatically shaded. Axial, sagittal, and coronal slices (between 22 and 29 slices per plane depending on globe dimensions) were then inspected and edited manually to rectify errors in automatic shading. The shading process was carried out twice for each MR data set.

Following shading, the procedure involved a shrink-wrapping process whereby a model of a sphere was first constructed using a mesh of 32,768 triangular polygons and the vertices of each polygon were shrunk toward the geometric center of the eye in an iterative fashion until each vertex intersected a shaded voxel. The corrugated shell generated was then smoothed, using local averaging of the vertex positions, to produce a vitreous–retina interface defined by a standardized $x$-$y$-$z$ 3D coordinate system for each of the 32,768 triangular polygons. The technique incorporated a system of unit vectors for each eye that provided a good approximation of the visual axis and an estimate of the longitudinal axial length (exclusive of the corneal thickness).[24]

The 32,768 $x$-$y$-$z$ coordinates representing the conformation of the vitreous–retina interface were assigned to principal quadrants (nasal, temporal, superior, and inferior, ~8200 data points per quadrant) and plotted in an $x$-$y$ plane to signify the composite shape of nasal, temporal, superior, and inferior quadrants (see inset in Fig. 1). The mean of each successive 10 data points was used to facilitate graphical representation and data analysis and thus the $y$-axis (designated the visual axis) comprised 820 data points.

## Graphical Representation of 2D MRI Coordinates for the Posterior Vitreous Chamber

The methods used to present and analyze data for all subjects and quadrants are described with reference to data for nasal and temporal quadrants of the right eye (RE) of subject BS with emmetropia (see Fig. 1).

The second nodal point (NP2) was adopted as a pivotal reference point for the measurement of posterior vitreous chamber dimensions, a procedure similar to that used in
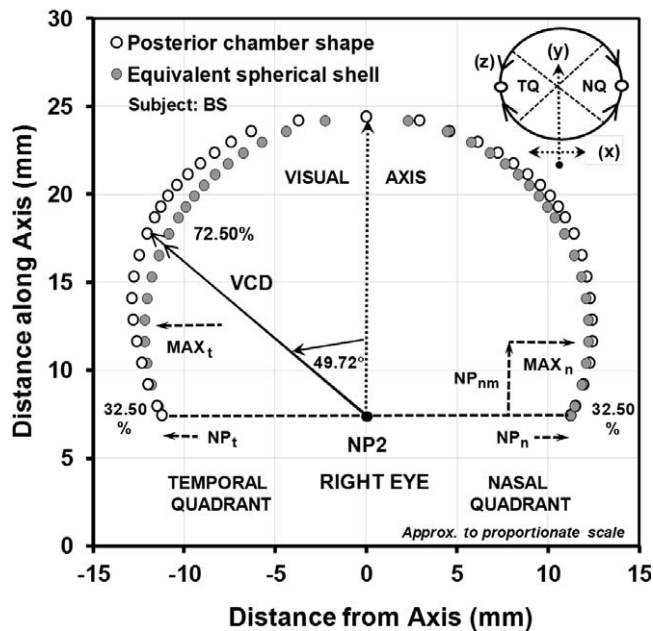
**FIGURE 1.** Posterior vitreous chamber shape across nasal and temporal quadrants plotted as distance along the visual axis (*y*-axis) against distance from the visual axis (*x*-axis) for RE (*open circles*) of representative subject BS with emmetropia (MSE −0.38 D, axial length 24.41 mm, female, age 19 years, British Asian). The inset diagram illustrates how (*z*)-axis data are amalgamated to form a two dimensional (*x*)-(*y*) plane, which represents posterior chamber shape of nasal and temporal quadrants. The mean distance from the visual axis is plotted against the midpoint of each successive interval, which represents 5% of the axial length between 30% and 75% (i.e., 32.5%, 37.5%, et seq.) and for each successive interval of 2.5% between 75% and 100% (i.e., 76.25%, 78.75%, et seq.) of axial length. VCD is the posterior chamber depth as measured from NP2, VCD along visual axis (0°) = 16.97 mm; VCD at NP2 (±90°) = ±11.22 mm. An equivalent spherical shell is plotted (*gray circles*) with dimensions based on the principal chord lengths obtained from MRI data for the actual eye. Width of the globe at NP2 (NP$_n$ + NP$_t$) is 22.44 (i.e., 11.22 × 2) mm. For subject BS maximum widths for nasal (MAX$_n$) and temporal (MAX$_t$) quadrants were 12.47 and 12.87 mm, respectively, giving a total temporal to nasal meridional width of 25.34 mm. The distances from NP2 to MAX$_n$ and MAX$_t$ (i.e., NP$_{nm}$ and NP$_{tm}$) were 4.58 and 6.36 mm, respectively (NP$_{tm}$ not shown).

previous studies investigating the effect of form deprivation on peripheral refractions and ocular shape in infant rhesus monkeys.[7] It was assumed that NP2 was located at the posterior pole of the crystalline lens and bisected the line representing distances from NP2 to the two adjacent vitreous–retina interfaces; the axis orthogonal to this line was coincident with the visual axis (see Fig. 1). The distance from the posterior pole of the cornea to NP2 (7.44 mm for subject BS) was taken as the sum of the ACD and lens thickness. A constant lens thickness of 3.75 mm was used for all subjects because this was obtained as a mean value for a similar subject sample and MRI protocol.[33] To satisfy the assumption regarding the location of NP2 required a small adjustment of nasal (NP$_n$) and temporal (NP$_t$) *x*-coordinates for subject BS (initially 10.96 and 11.48 mm, respectively) of ±0.26 mm, which gave a bisected value of 11.22 mm.

In Figure 1 the 2D graphical representation of MRI coordinates is restricted to the posterior vitreous chamber that extends from 30% to 100% of axial length. The mean distance from the visual axis is plotted against the midpoint of each successive interval that represents 5% of the axial length

between 30% and 75% (i.e., 32.5%, 37.5% et seq.) and, to account for the increased rate of curvature, for each successive interval of 2.5% between 75% and 100% (i.e., 76.25%, 78.75% et seq.) of axial length. The 30% to 100% proportion of axial length is therefore represented by 574 data points (i.e., 820 × 0.7) and hence the mean values (M) of data falling within the 5% and 2.5% intervals are each derived from approximately 40 and 20 data points, respectively. To provide an example of the level of variation of data within intervals the mean values for subject BS were combined with corresponding standard deviations (SD) to calculate the coefficient of variation (CoV; CoV% = [SD/M] × 100) for each successive percentage data point. Mean CoVs (range) for the nasal and temporal quadrants were 2.28% (0.30%–6.47%) and 1.81% (0.37%–5.09%)%, respectively. Maximum CoVs occurred in the posterior 5% of axial length (approximately 1.22 mm for subject BS) owing to the effect of voxel dimensions on the values of *x* as the maximum value of *y* is approached.

**Construction of the Equivalent Spherical Shell.** NP2 was used as a reference point to plot, for the posterior chamber, a sphere segment with dimensions based on the principal chord lengths obtained from the MRI for the actual eye. Thus the sphere segment in Figure 1 is constructed from a principal *x*-axis semichord length of 11.22 (10.96 + 11.48)/2) mm and a principal *y*-axis semichord length of 16.97 mm (i.e., the difference between MRI axial length [24.41mm] and the location of NP2 [7.44mm]). The segment, referred to henceforth as the equivalent spherical shell, can be considered a spherical analogue of posterior chamber shape and is used to compare relative sphericity between quadrants (see Supplementary Fig. S1 and Calculations for details of the geometry and trigonometry used to calculate the dimensions of the equivalent spherical shell).

## Dimensions of the Posterior Vitreous Chamber

**Vitreous Chamber Depth for the Actual Eye and Its Spherical Equivalent.** As illustrated in Figure 1, vitreous chamber depths (VCDs) were measured from NP2 for the equivalent spherical shell and the actual eye to provide single successive measurements of VCD for angles subtended at data points representing successive percent distances along the axis (see Fig. 2A). The mean of VCDs summed over quadrants (i.e., ±0°–90°) was used as an output variable for statistical analysis.

The ratio of actual VCD to equivalent spherical shell VCD (designated the actual to sphere VCD ratio) was calculated and plotted in Figure 2B. The ratio was used to compare the profile of relative sphericity between quadrants because a constant ratio of 1 indicates that chamber shape is spherical (see Supplementary Fig. S1 and Calculations for details of the geometry and trigonometry used to calculate the actual to sphere VCD ratio). The mean of actual to sphere VCD ratios summed over quadrants (i.e., ±0°–90°) was used as an output variable for statistical analysis. Second order polynomials were fitted to data points between 32.5% and 98.5% (inclusive) for each quadrant in Figure 2B and differentiated to calculate from the derivative dy/dx = 0 the angular subtense that corresponded to the maximum actual to sphere VCD ratio.

**Dimensions Across Quadrants and Globe.** The distance across the globe at NP2 has been referred to earlier and is taken as the sum of NP$_n$ and NP$_t$ (where NP$_n$ = NP$_t$, see Fig. 1). Maximum distance from the visual axis was calculated for the nasal (MAX$_n$) and temporal (MAX$_t$) quadrants by fitting second order polynomial curves to data points in Figure 1 between 32.5% and 72.5% (inclusive) of axial length and differentiating the equations to determine from the derivative dy/dx = 0 the value of the *x*-coordinates corresponding to maximum distances. The sum of maximum distances for nasal and
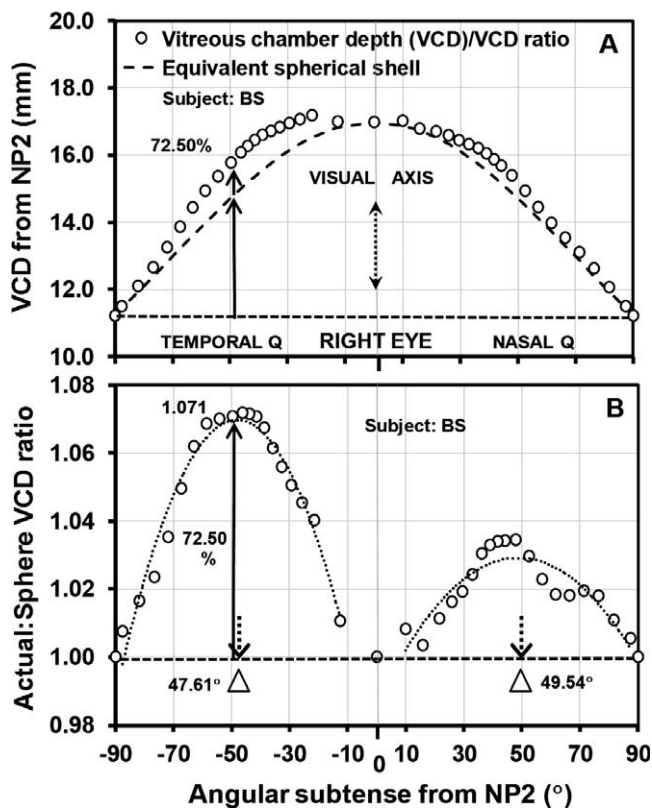
**FIGURE 2.** (**A**) VCDs for the actual eye (*open circles*) and equivalent spherical shell (represented as a *dashed line* rather than separate data points) for angles subtended at data points representing successive % distances along the axis in Figure 1. For the 72.5% point (angular subtense from NP2 = 49.72°) highlighted in Figure 1 VCDs for the actual eye and equivalent spherical shell were 15.77 and 14.73 mm, respectively and the means of summed VCDs over nasal and temporal quadrants ($\pm0°$ to 90°) were 14.92 and 15.31 mm, respectively. (**B**) Actual to sphere VCD ratios calculated from Figure 2A and plotted for angles subtended at data points representing successive % distances along the axis. For the 72.5% point highlighted the actual to sphere VCD ratio was 1.071 (15.77/14.73 mm) and the means of summed actual to sphere VCDs over nasal and temporal quadrants ($\pm0°$ to 90°) were 1.017 and 1.053, respectively. Differentiation of second order polynomials fitted between 32.5% and 98.5% (*dotted line*) for nasal ($R^2 = 0.78$) and temporal quadrants ($R^2 = 0.97$) indicated the maximum ratios to occur at 49.54° and 47.61°, respectively (*open triangles*).

temporal quadrants is designated the maximum temporal to nasal meridional distance. Distance $NP_{nm}$ in Figure 1 represents the distance from NP2 to the point of maximum orthogonal distance from the visual axis for the nasal quadrant and is the difference between the $y$-coordinate corresponding to maximum distance from the $y$-axis and the $y$-coordinate for NP2.

Since a previous study used T1-weighted MR images to fit ellipsoids to retinal shape,[23] it was of interest to examine whether the shape of the posterior chamber extending from points of maximum quadrant width to the fovea could be considered elliptical. Therefore, Figure 3 confines the plot in Figure 1 to the percentage data point adjacent to the maximum quadrant widths found for subject BS (i.e., 57.5%). The maximum distance from the visual axis for the nasal quadrant adopted as the semiprincipal axis $a$ of an ellipse and corresponding semiprincipal axis $b$ is given by the difference between the $y$-coordinate for the MRI axial length and $y$-coordinate corresponding to maximum distance from the $y$-axis. Using the
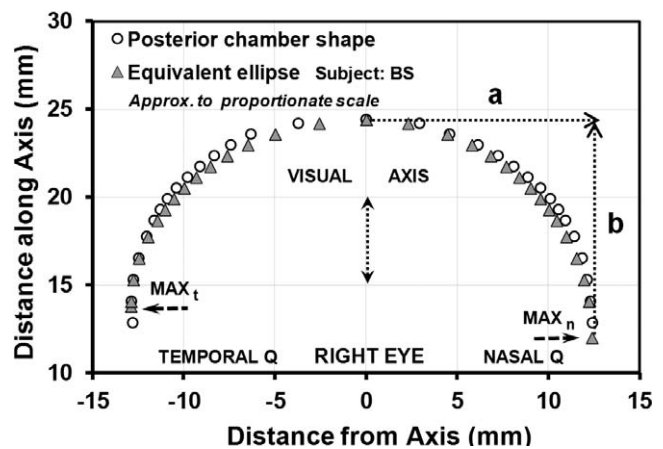


**FIGURE 3.** Posterior chamber shape as plotted in Figure 1 for subject BS for 57.5% to 100% of chamber depth (*open circles*). Values of $a$ and $b$ for the nasal quadrant were 12.47 and 12.39 mm and for the temporal quadrant 12.87 and 10.60 mm giving $a$ to $b$ ratios of 1.01 and 1.21, respectively. Values $a$ and $b$ were used to plot equivalent ellipses (*gray triangles*) using the standard equation for an ellipse: $\frac{(x-x_o)^2}{a^2} + \frac{(y-y_o)^2}{b^2} = 1$ where $x_o = 0$ and $y_o$ = distance along $y$-axis from the origin (i.e., posterior corneal surface) to the point of maximum globe width; $a$ = maximum globe width; $b$ = distance along $y$-axis from point of maximum globe width to fovea.

standard equation for an ellipse, Figure 3 plots ellipses for nasal and temporal quadrants using respective values of semiprincipal axes $a$ and $b$ and demonstrates that actual plots and ellipse plots for subject BS are contiguous.

The graphical representations and data analyses described above for subject BS were carried out on all subjects for all four quadrants of both eyes using MRI coordinates generated from two separate MRI shading procedures.

### Statistical Analyses

Statistical analyses were conducted using IBM SPSS Statistics 20 (IBM UK, Ltd., Portsmouth, UK). The level of statistical significance was taken as 5% and calculation of 95% confidence intervals used a two-tailed $t$-value. Mixed-design repeated measures ANOVAs were used to test differences in outcome variables for the between-subject factor refractive group (two levels: myopia and emmetropia) and for the within-subject factors eye (two levels: right and left) and quadrant (four levels: nasal, temporal, superior, and inferior). Simple contrasts were used for statistical comparisons of within-subject factors and their interactions. Distributions of data were checked for normality using the Shapiro-Wilk test and equality of variances and sphericity were tested using the Levene and Mauchly tests, respectively. Differences in age between refractive groups were tested with a $t$-test (two-tailed) and differences in distribution of sex and ethnicity were tested with the Pearson's $\chi^2$ test (two-sided).[34]

### RESULTS

#### Subjects

Fifty-five subjects were enlisted, 27 with emmetropia and 28 with myopia. Neither age ($P = 0.88$) nor distributions of sex ($P = 0.06$) and ethnicity ($P = 0.774$) were significantly affected by refractive grouping (Table 1).

**TABLE 1.** Intergroup Comparisons of Demography of Subjects Recruited

|  | Emmetropia, $N = 27$ | Myopia, $N = 28$ |
|---|---|---|
| Age, y | 25.81 ± 6.77 | 25.57 ± 5.00 |
| Sex | F: 16; M: 11 | F: 23; M: 5 |
| Ethnicity | AC: 2; BSA: 11; BW: 14 | BSA: 10; BW: 15; C: 3 |

Mean values ± 1 SD. F, female; M, male. AC, African-Caribbean; BSA, British South Asian; BW, British White; C, Chinese.

## Ocular Biometry

The mean level of myopia (REs and left eyes [LEs] combined) was 5.87 D MSE (Table 2). The significant difference ($P = 0.009$) in MSE between RE and LE of subjects with myopia is attributed to 6 of the 28 subjects exhibiting more than 2 D anisomyopia in the RE (mean = 2.40 D, range 2.00–2.80 D MSE). Statistical analyses of data for REs and LEs have therefore been carried out separately except for ratio data for which additional intereye comparisons have been made. The mean cylindrical correction for the whole data set was −0.55 ± 0.53 D with no significant differences between eyes or refractive group.

Combining data for RE and LE the mean corneal radius was significantly steeper in myopia than in emmetropia (−0.30 mm; $P < 0.001$), but the corresponding increase in ocular power was partly offset by the significantly greater mean anterior chamber depth (0.31 mm; $P < 0.001$), which in turn located NP2 0.31 mm more posteriorly than in emmetropia. As expected, axial lengths and VCDs were significantly greater in myopia ($P < 0.001$). Taking partial coherence interferometry (PCI) as the standard reference measurement, it is likely that the longer mean axial length estimated with MRI is a consequence of the tight binding of the mesh to the outside of the 1 by 1 by 1 mm voxels acquired in the MRI shrink-wrapping process.[24] MRI measurement of axial length was significantly correlated with PCI measurement in both eyes (RE: $y$ [PCI] $= 0.87x + 3.60$ [$R^2 = 0.86$; $P < 0.001$]; LE: $y$ [PCI] $= 0.92x + 1.54$ [$R^2 = 0.81$; $P < 0.001$]), and a difference of means analysis[34] indicated mean MRI axial length of the RE to be 0.35 mm greater than PCI axial length (LE +0.58 mm) with a 95% confidence interval of 0.89 mm for differences between MRI and PCI axial lengths (LE 1.01 mm). The correlation between MRI axial length and MSE was highly significant for both REs ($y$ [MRI] $= 0.28x + 24.21$ [$R^2 = 0.63$; $P < 0.001$]) and LEs ($y$ [MRI] $= 0.29x + 24.42$ [$R^2 = 0.59$; $P < 0.001$]) and was consistent with those previously reported using MRI.[22] MRI axial length does not include corneal thickness (~0.55 mm) because measurements are taken from the posterior surface of the cornea to the fovea.

## MR Image Acquisition

**Repeatability of Shading Procedure.** The shading procedure was repeated (author MN) on five separate occasions (masked) for the RE of an individual with emmetropia (subject AC, MSE −0.19 D). The CoVs of $x$-axis distances from the visual axis were calculated for each percentage data point between 32.5% and 98.50%. The mean CoV % of all 18 points combined for nasal, temporal, superior, and inferior quadrants was 3.04, 3.50, 5.46, and 4.49, respectively. The mean estimated axial length was not significantly affected by repeat shading (mean = 23.35, range 23.32–23.37 mm).

## Graphical Representation of 2D MRI Coordinates for the Posterior Vitreous Chamber

**Adjustment to Location of NP2.** The adjustments required to $x$-coordinates to satisfy the properties of NP2 were calculated for all subjects (Table 3) and were small, representing on average 1% of total globe width at NP2. For the RE no

**TABLE 2.** Intergroup and Interocular Comparisons of Refractive and Biometric Data for Subjects With Emmetropia ($N = 27$) and Myopia ($N = 28$)

|  | Right Eye | Left Eye |
|---|---|---|
| **MSE, D** |  |  |
| Emmetropia | +0.06 ± 0.36 (−0.55 to +0.69) | +0.12 ± 0.36 (−0.44 to +0.75) |
| Myopia | −6.22 ± 2.38 (−2.31 to −10.05) | −5.52 ± 2.25 (−2.00 to −9.31) |
| **Corneal radius, mm** |  |  |
| Emmetropia | 7.88 ± 0.22 (7.37 to 8.38) | 7.87 ± 0.19 (7.41 to 8.34) |
| Myopia | 7.57 ± 0.26 (6.95 to 8.21) | 7.57 ± 0.26 (6.92 to 8.21) |
| **ACD, mm** |  |  |
| Emmetropia | 3.44 ± 0.22 (3.04 to 3.76) | 3.45 ± 0.25 (2.94 to 3.93) |
| Myopia | 3.70 ± 0.25 (3.15 to 4.07) | 3.76 ± 0.27 (3.27 to 4.27) |
| **NP2, mm** |  |  |
| Emmetropia | 7.19 ± 0.22 (6.75 to 7.51) | 7.20 ± 0.25 (6.69 to 7.68) |
| Myopia | 7.45 ± 0.25 (6.90 to 7.82) | 7.51 ± 0.27 (7.02 to 8.02) |
| **Axial length: PCI, mm** |  |  |
| Emmetropia | 23.66 ± 0.62 (22.44 to 25.26) | 23.64 ± 0.64 (22.48 to 25.19) |
| Myopia | 25.78 ± 0.97 (23.33 to 27.99) | 25.57 ± 0.98 (23.64 to 27.64) |
| **Axial length: MRI, mm** |  |  |
| Emmetropia | 24.14 ± 0.73 (22.75 to 25.36) | 24.35 ± 0.79 (23.12 to 26.26) |
| Myopia | 26.02 ± 0.99 (23.98 to 28.34) | 26.04 ± 1.04 (24.15 to 28.05) |
| **Vitreous chamber depth: MRI, (0°) mm** |  |  |
| Emmetropia | 16.94 ± 0.72 (15.68 to 18.48) | 17.13 ± 0.79 (16.02 to 18.85) |
| Myopia | 18.57 ± 1.01 (16.36 to 21.08) | 18.54 ± 1.04 (16.56 to 20.85) |

Mean values ± 1 standard deviation (range).

**TABLE 3.** Intergroup, Interocular, and Interquadrant Comparisons of MRI Data

| | Right Eye | | | | Left Eye | | | |
|---|---|---|---|---|---|---|---|---|
| | Temporal | Nasal | Inferior | Superior | Temporal | Nasal | Inferior | Superior |
| **Adjustment to NP2, ± mm** | | | | | | | | |
| Emmetropia | 0.006 ± 0.21 | | 0.27 ± 0.13 | | 0.41 ± 0.11 | | 0.31 ± 0.15 | |
| Myopia | −0.13 ± 0.19 | | 0.31 ± 0.17 | | 0.29 ± 0.21 | | 0.39 ± 0.19 | |
| **Mean of summed VCDs, mm, ±0°–90°** | | | | | | | | |
| Emmetropia | 15.25 ± 0.53 | 14.97 ± 0.53 | 15.14 ± 0.58 | 15.31 ± 0.50 | 15.18 ± 0.54 | 15.40 ± 0.56 | 15.32 ± 0.59 | 15.38 ± 0.60 |
| Myopia | 16.11 ± 0.76 | 15.91 ± 0.82 | 16.06 ± 0.77 | 16.07 ± 0.76 | 15.79 ± 0.72 | 16.11 ± 0.82 | 16.08 ± 0.74 | 16.07 ± 0.79 |
| **Mean of summed actual to sphere VCD ratios, mm, ±0°–90°** | | | | | | | | |
| Emmetropia | 1.040 ± 0.018 | 1.017 ± 0.013 | 1.026 ± 0.013 | 1.039 ± 0.021 | 1.024 ± 0.015 | 1.039 ± 0.013 | 1.031 ± 0.014 | 1.035 ± 0.018 |
| Myopia | 1.019 ± 0.013 | 1.003 ± 0.015 | 1.013 ± 0.015 | 1.012 ± 0.015 | 1.009 ± 0.017 | 1.024 ± 0.016 | 1.016 ± 0.016 | 1.015 ± 0.014 |
| **Mean distance across globe from NP2, 90°, mm** | | | | | | | | |
| Emmetropia | 22.54 ± 0.60 | | 22.71 ± 0.62 | | 22.54 ± 0.55 | | 22.62 ± 0.67 | |
| Myopia | 22.61 ± 0.85 | | 22.62 ± 0.74 | | 22.45 ± 0.10 | | 22.61 ± 0.99 | |
| **Maximum globe dimensions for temporal to nasal and inferior to superior meridians, mm** | | | | | | | | |
| Emmetropia | 25.33 ± 0.69 | | 25.67 ± 0.81 | | 25.56 ± 0.69 | | 25.77 ± 0.85 | |
| Myopia | 25.80 ± 0.95 | | 25.94 ± 0.94 | | 25.85 ± 1.06 | | 26.03 ± 0.98 | |
| **Distances from NP2 to the point of maximum orthogonal distance from the visual axis, mm** | | | | | | | | |
| Emmetropia | 5.71 ± 0.50 | 5.08 ± 0.39 | 5.28 ± 0.45 | 5.57 ± 0.46 | 5.45 ± 0.57 | 5.62 ± 0.55 | 5.52 ± 0.59 | 5.73 ± 0.60 |
| Myopia | 6.37 ± 0.61 | 5.87 ± 0.71 | 6.00 ± 0.76 | 6.04 ± 0.66 | 6.11 ± 0.67 | 6.27 ± 0.81 | 6.14 ± 0.69 | 6.22 ± 0.68 |
| **Maximum orthogonal distances from visual axis, mm, semiprincipal axis *a*** | | | | | | | | |
| Emmetropia | 12.83 ± 0.38 | 12.50 ± 0.35 | 12.77 ± 0.47 | 12.91 ± 0.40 | 12.66 ± 0.36 | 12.90 ± 0.36 | 12.87 ± 0.46 | 12.90 ± 0.43 |
| Myopia | 13.00 ± 0.47 | 12.80 ± 0.53 | 12.96 ± 0.49 | 12.98 ± 0.47 | 12.83 ± 0.52 | 13.02 ± 0.56 | 12.99 ± 0.48 | 13.05 ± 0.53 |
| **Distances along the axis from the point of maximum orthogonal distance from the visual axis, mm, semiprincipal axis *b*** | | | | | | | | |
| Emmetropia | 11.26 ± 0.69 | 11.89 ± 0.63 | 11.69 ± 0.44 | 11.42 ± 0.81 | 11.73 ± 0.55 | 11.54 ± 0.52 | 11.68 ± 0.60 | 11.48 ± 0.69 |
| Myopia | 12.19 ± 0.64 | 12.70 ± 0.55 | 12.56 ± 0.75 | 12.52 ± 0.77 | 12.43 ± 0.73 | 12.26 ± 0.72 | 12.39 ± 0.71 | 12.32 ± 0.62 |
| ***a* to *b* ratio** | | | | | | | | |
| Emmetropia | 1.14 ± 0.07 | 1.05 ± 0.04 | 1.09 ± 0.04 | 1.14 ± 0.08 | 1.08 ± 0.05 | 1.12 ± 0.05 | 1.10 ± 0.06 | 1.13 ± 0.07 |
| Myopia | 1.07 ± 0.05 | 1.01 ± 0.05 | 1.04 ± 0.06 | 1.04 ± 0.06 | 1.03 ± 0.06 | 1.06 ± 0.05 | 1.05 ± 0.05 | 1.06 ± 0.05 |

Mean values ± 1 SD.

significant differences in adjustment were found between refractive groups ($P = 0.11$), but adjustments for the temporal to nasal quadrants were significantly different from those for inferior to superior quadrants ($P < 0.001$). The significant interaction between refractive group and quadrant combination ($P = 0.02$) were attributable to the smaller adjustments required for the temporal to nasal quadrant for both emmetropia and myopia. For the LE no significant differences in adjustment were found between refractive groups ($P = 0.43$) or quadrants ($P = 0.99$). There was a significant interaction, however, between refractive group and quadrant combination ($P = 0.007$) because adjustment values were larger in emmetropia for the temporal to nasal quadrant but smaller for the inferior to superior quadrant.

Figure 4 replots Figure 1 for REs and LEs of both refractive groups and all quadrants. In addition to confirming the well-documented finding that posterior vitreous chamber dimensions in myopia are enlarged compared with emmetropia, there was clear evidence of regional differences in chamber shape in relation to the equivalent spherical shell plots.

## Dimensions of the Posterior Vitreous Chamber

**Vitreous Chamber Depths for the Actual Eye and Its Spherical Equivalent.** Figures 5 and 6 replot Figures 2A and 2B for the whole data set, Figure 5 for nasal and temporal quadrants, and Figure 6 for superior and inferior quadrants. The mean of VCDs summed between 0° and 90° for each quadrant are shown in Table 3 (see Figs. 5A, 5B, 6A, 6B). Differences between refractive groups and between quadrants were significant for both REs and LEs (all $P < 0.001$) but the interactions between refractive group and quadrant were insignificant (RE, $P = 0.12$; LE, $P = 0.11$). Within-subject contrasts indicated that the significant difference between quadrants was attributable principally to the differences between nasal and temporal quadrants (RE, $P < 0.001$; LE, $P < 0.001$) and temporal and inferior quadrants (RE, $P = 0.003$; LE, $P < 0.001$).

The mean of actual to sphere ratios summed between 0° and 90° for each quadrant are shown in Table 3 (see Figs. 5C, 5D, 6C, 6D). The Shapiro-Wilk test was used to confirm that ratio data were normally distributed. There were no significant differences in ratios between eyes ($P = 0.148$). Differences between refractive groups and between quadrants were significant ($P < 0.001$ and $P = 0.025$, respectively). The interactions between eye and quadrant and refraction and quadrant were significant ($P < 0.001$ and $P = 0.015$, respectively). In summary, within-subject contrasts and inspection of Figures 5C, 5D, 6C, and 6D showed that these interactions were most likely attributable to the intereye reversal of peak ratios between nasal and temporal quadrants for both emmetropia and myopia (Figs. 5C, 5D, see later
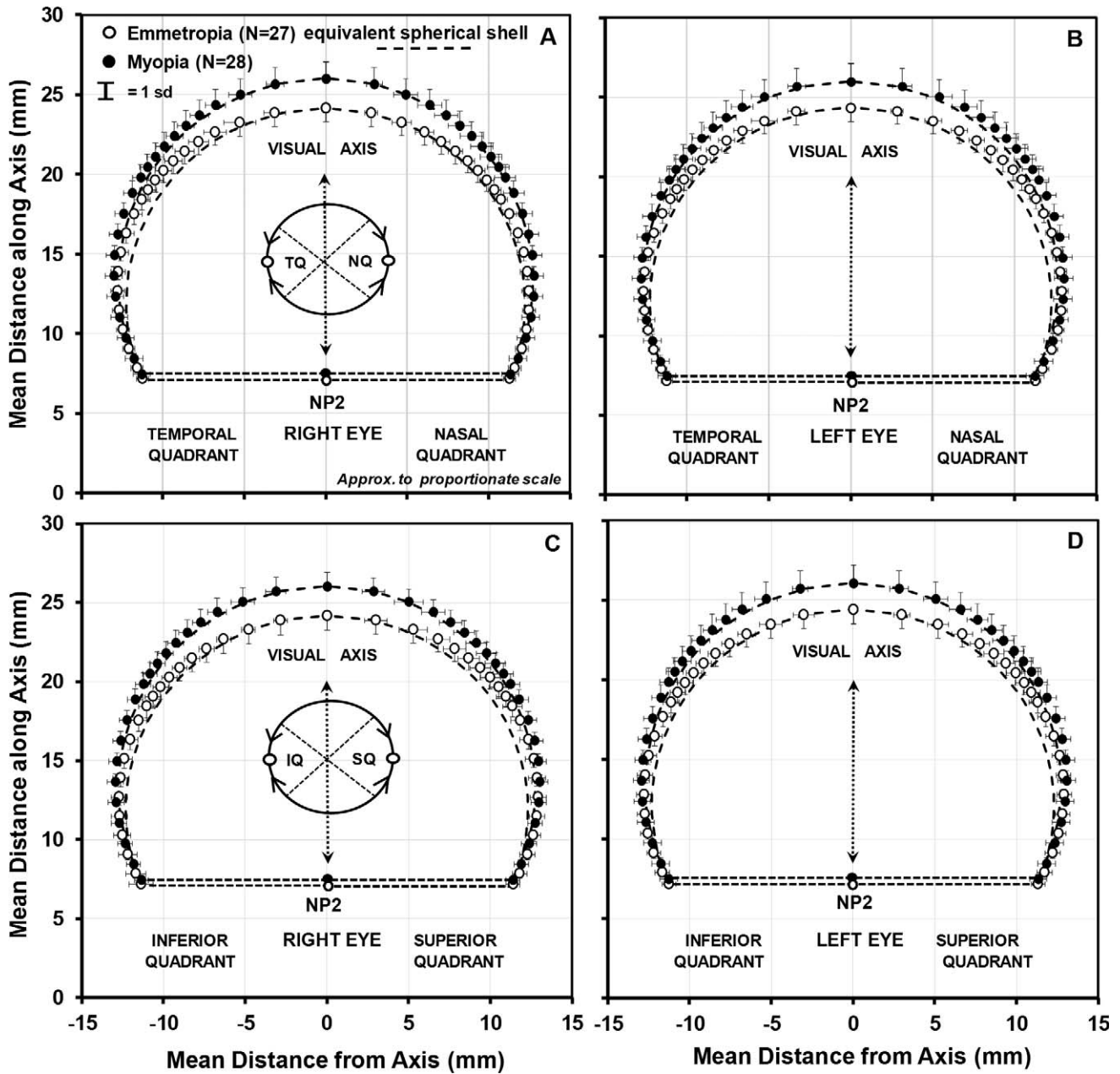
**FIGURE 4.** Posterior chamber shape as plotted in Figure 1 for all quadrants of the RE and LE of subjects with emmetropia (*open circles*, $N = 27$) and subjects with myopia (*filled circles*, $N = 28$). (**A, B**) Temporal to nasal quadrants of RE and LE; (**C, D**) inferior to superior quadrants of RE and LE. The *vertical* and *horizontal error bars* represent the variation between subjects in distance along the axis and distance from the axis for each successive interval representing 5% of the axial length between 30% and 75% and of 2.5% between 75% and 100%. For expediency the equivalent spherical shell plots are represented as a *dashed line* rather than individual data points as shown in Figure 1.

comment) and the relatively low ratios found for the nasal quadrant of the RE in both emmetropia and myopia (Fig. 5C).

Angular subtenses that corresponded to maximum actual to sphere VCD ratios were calculated for each subject by differentiation of second order polynomials as described in the Methods section. The mean (range) $R^2$ values (eyes and quadrants combined) for subjects with emmetropia that could be fitted (95% of the sample) was 0.89 (0.99-0.58) and for subjects with myopia that could be fitted (61% of the sample) was 0.78 (0.98-0.34). Angular subtenses are shown in Figures 5C, 5D, 6C, and 6D (lower section) and were significantly different between refractive groups ($P < 0.001$) but not

between eyes or quadrants ($P = 0.679$ and $P = 0.213$, respectively). Mean angular subtense (eyes and quadrants combined) was 52.38° (±5.12) for emmetropia and 49.67° (±8.26) for myopia. The interaction between refractive group and quadrant was found to be significant ($P = 0.004$) and within-subject contrasts showed this to be attributable to the differences between superior and inferior quadrants ($P = 0.004$), which is evident in a comparison of the differences in angular subtenses between emmetropia and myopia in Figures 6C and 6D.

Intereye comparison of nasal and temporal data suggests an amalgamation of posterior chamber shape into right and
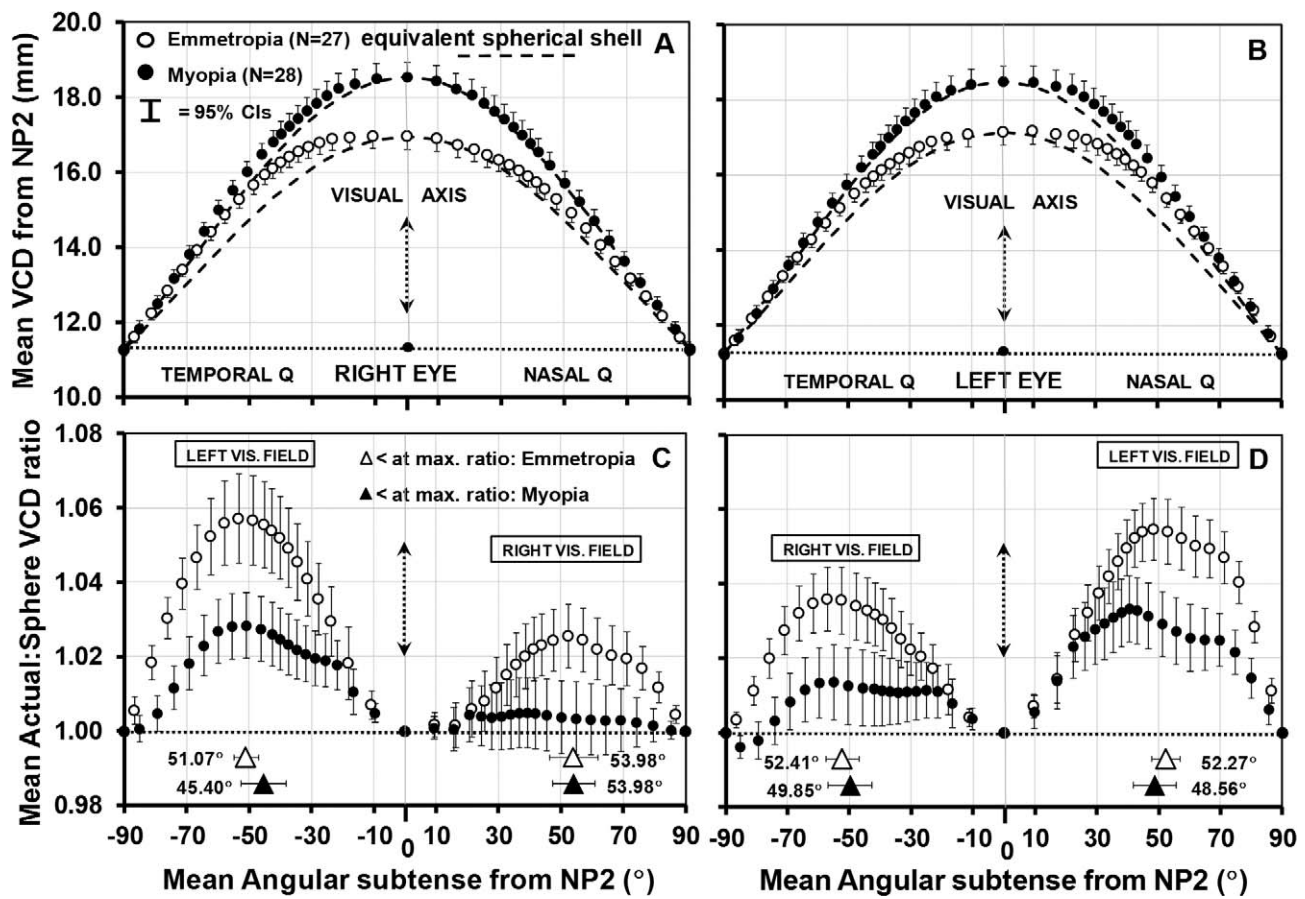
**FIGURE 5.** Figures 2A and 2B replotted for the whole data set for nasal and temporal quadrants. (**A**, **B**) VCDs for the nasal and temporal quadrants of the RE and LE, respectively. The equivalent spherical shell plots for each condition are represented as a dashed line. (**C**, **D**) Actual to sphere VCD ratios for the nasal temporal quadrants of the RE and LE, respectively. Also shown are the x-coordinates of the mean ($\pm$ 1 SD) angular subtense corresponding to the mean maximum value for actual to sphere ratio. *Horizontal error bars* for angular subtense have been omitted for expediency but were of the order of $\pm 1.8°$ (SD). Indicated is the amalgamation of quadrants into the right and left visual fields; that is, right nasal quadrant is coupled with left temporal quadrant and right temporal quadrant is coupled with left nasal quadrant, respectively.

left visual fields. For example, the mean summed actual to sphere VCD ratios for the nasal quadrant in myopia and emmetropia are less than those for the temporal quadrant in the RE but greater in the LE (Table 3) a difference that is evident in a comparison of the profile of ratios in Figures 5C and 5D. A similar reversal between the RE and LE was not apparent in a comparison of mean summed actual to sphere VCD ratios for superior and inferior quadrants (Table 3, Figs. 6C, 6D).

**Dimensions Across Quadrants and Globe (See Fig. 1).** Table 3 compares the mean distances across the globe at NP2 for temporal to nasal and inferior to superior quadrants. There were no significant differences in distances between refractive groups (RE, $P = 0.95$; LE, $P = 0.85$) or between quadrants (RE, $P = 0.42$; LE, $P = 0.062$).

Table 3 compares the mean maximum dimensions between temporal to nasal and superior to nasal meridians. There were no significant differences between refractive groups for either the RE ($P = 0.12$) or LE ($P = 0.24$), but significant differences between meridians (i.e., the inferior to superior meridian) were on average greater than the temporal to nasal meridian by 0.24 mm in the RE ($P < 0.001$) and 0.20 mm in the LE ($P = 0.005$). There was no significant interaction between differences in meridians and refractive group (RE, $P = 0.84$; LE, $P = 0.80$).

Table 3 compares the mean distances from NP2 to the point of maximum orthogonal distance from the visual axis. Mean distances were significantly greater ($P < 0.001$) in myopia than in emmetropia for both REs (0.66 mm) and LEs (0.60 mm) and significantly different between quadrants (both eyes, $P < 0.001$). The interaction between quadrant and refractive group just reached significance for the RE ($P = 0.05$) but was not significant for the LE ($P = 0.332$). Within-subjects contrasts for quadrant and the refractive group to quadrant interaction did not reveal any consistent pattern.

Figure 7 replots Figure 3 for all subjects and conditions. The mean maximum quadrant distances (i.e., semiprincipal axes $a$) were calculated for each subject by differentiation of second order polynomials as described in the Methods section and are shown in Table 3; all $R^2$ values exceeded 0.9. There were no significant differences between refractive groups (RE, $P = 0.12$; LE, $P = 0.24$), but differences between quadrants were significant for both REs and LEs (both $P < 0.001$). Within-subject contrasts failed, however, to show any significant pattern between eyes with regard to differences in maximum quadrant distances. There was no significant interaction between quadrants and refractive group (RE, $P = 0.06$; LE, $P = 0.82$).

Mean values for semiprincipal axis $b$ are given in Table 3. Significant differences were found between refractive groups and quadrants for REs and LEs (all $P < 0.001$). The former was
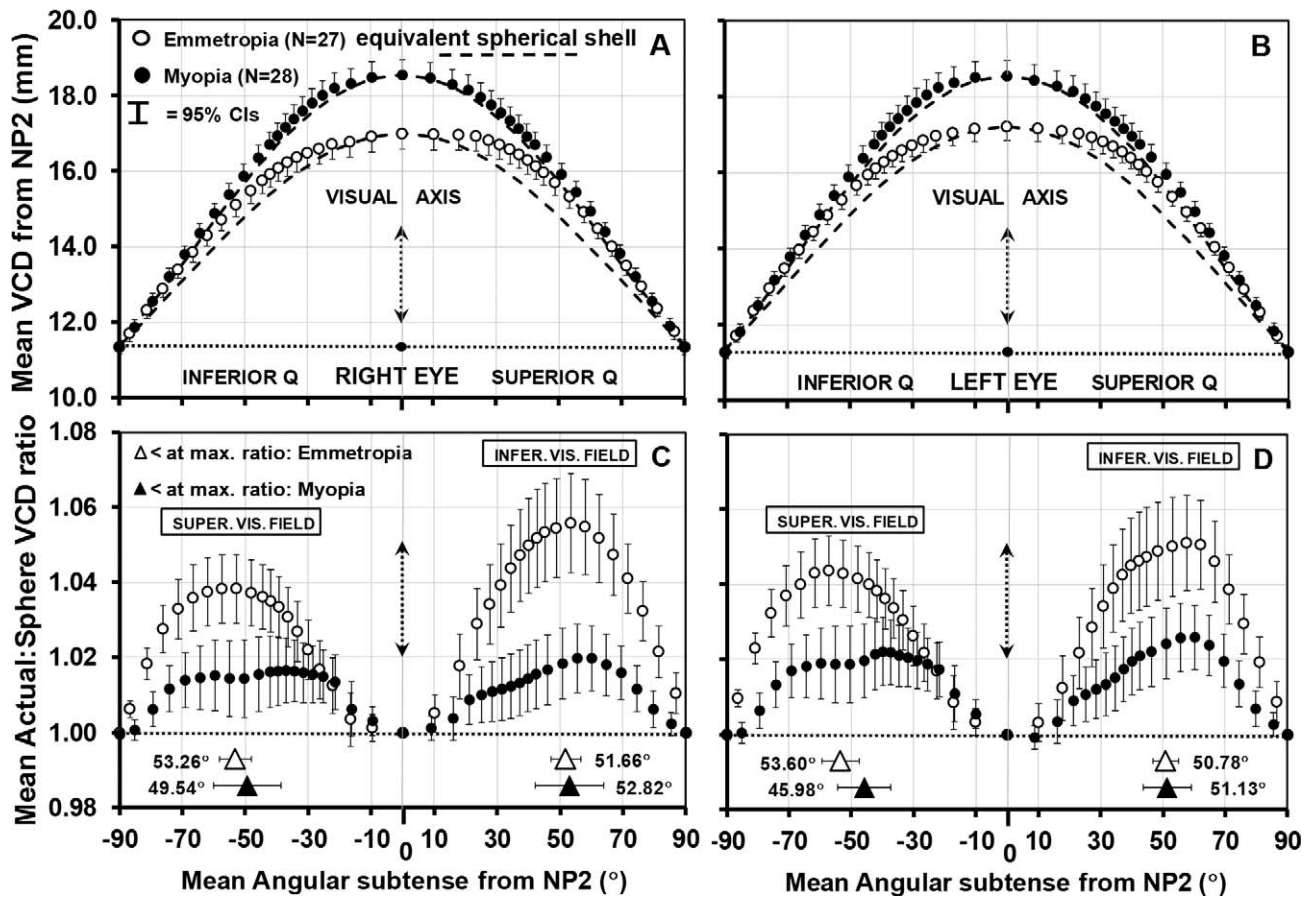
**FIGURE 6.** Figures 2A and 2B replotted as in Figure 5 for superior and inferior quadrants. (**A**, **B**) VCDs for the superior and inferior quadrants of the RE and LE, respectively. The equivalent spherical shell plots for each condition are represented as a *dashed line*. (**C**, **D**) Actual to sphere VCD ratios for the superior and inferior quadrants of the RE and LE. Also shown are the *x*-coordinates of the mean (± 1 SD) angular subtense corresponding to the mean maximum value for actual to sphere ratio. *Horizontal error bars* for angular subtense have been omitted for expediency but were of the order of ±1.8° (SD). Indicated is the amalgamation into the superior and inferior visual fields; that is, right inferior quadrant is coupled with left inferior quadrant and right superior quadrant is coupled with left superior quadrant, respectively.

to be expected, but no clear pattern emerged from analyses of within-subject contrasts for the latter.

The mean values of semiprincipal axes *a* and *b* displayed in Figure 7 were used to generate ellipses as described in the Methods section. Of note is that the equivalent ellipses are contiguous with actual plots for all conditions, that is, 2D representation of posterior chamber shape can generally be considered to match that of an ellipse. Ellipses can be defined as prolate (*a* < *b*; ratio < 1) or oblate (*a* > *b*; ratio > 1), which allows posterior chamber shape to be described qualitatively with reference to the mean *a* to *b* ratios shown in Table 3. The Shapiro-Wilk test was used to confirm that all ratio data were normally distributed. Differences in ratios between eyes were not significant ($P = 0.095$), but mean ratios for myopia were significantly lower than for emmetropia ($P < 0.001$). Thus, as previously apparent from Figures 4, 5, and 6, myopic eyes are more spherical than emmetropic eyes. A prolate shape does not, however, appear to be a feature of myopic eyes because ratios rarely fell below 1. Differences in ratios between quadrants were significant ($P < 0.001$). The interaction between eye and quadrant was significant ($P < 0.001$), but no clear pattern emerged from analyses of within-subject contrasts for the interaction. The interaction between refractive group and quadrant was not significant ($P = 0.06$).

## DISCUSSION

Plots of posterior vitreous chamber shapes for emmetropia and myopia in Figure 4 demonstrate the well-established finding that the principal structural correlate of myopia is elongation of axial length.[35,36] The mean difference in length between myopia and emmetropia for the whole data set combined was 1.79 mm, which, for a mean difference in MSE of 5.78 D, converts to 0.31 mm/D, a ratio consistent with a previous MRI study (0.35 mm/D).[22] In addition, the juxtaposition of actual and equivalent spherical shell plots in Figure 4 is significantly closer in myopia than in emmetropia; that is, the myopic eye is more spherical than the emmetropic eye.

The differences between refractive groups in posterior chamber shape are compared more directly in Figures 5 and 6 using single measures of actual and equivalent spherical shell VCDs and their ratios. Figures 5A, 5B, 6A, and 6B illustrate, relative to equivalent spherical shells, that a more spherical shape occurs in myopia for both the temporal to nasal quadrants and inferior to superior quadrants of both eyes. Also evident is a discrepancy between actual and equivalent spherical shell VCDs in equatorial regions of emmetropic eyes that, with respect to right and left eyes, is asymmetric for temporal to nasal quadrants (Figs. 5A, 5B) but symmetric for superior to nasal quadrants (Figs. 6A, 6B).
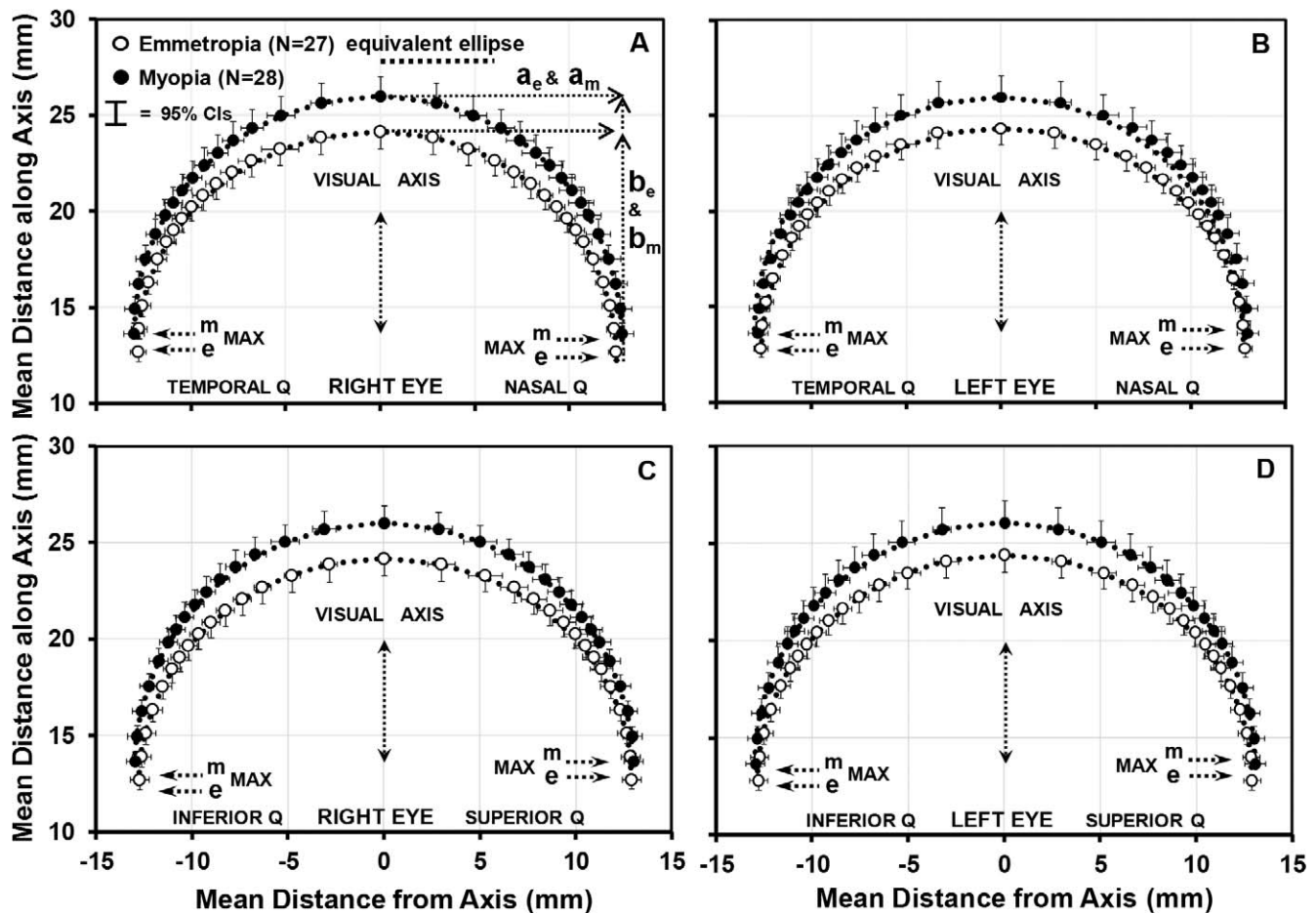
FIGURE 7. Posterior chamber shape plotted as in Figure 3 for the whole data set. (A, B) Temporal to nasal quadrants of RE and LE; (C, D) inferior to superior quadrants of RE and LE. Ellipse plots for emmetropia and myopia are calculated from the mean values of semiprincipal axes $a_e$ and $b_e$ and $a_m$ and $b_m$, respectively, and for expediency are represented as *dotted lines* rather than individual data points shown in Figure 3. MAX e and MAX m indicate the mean distances from the posterior corneal pole to the point of maximum orthogonal distance from the visual axis for emmetropia and myopia, respectively.

The profiles of actual to sphere VCD ratios illustrate further the intereye discrepancy in equatorial regions. Profiles were shown to be reversed for temporal to nasal quadrants of both refractive groups (Figs. 5C, 5D) but were similar for inferior to superior quadrants (Figs. 6C, 6D). Given the bifurcation of nasal and temporal retinal fibers into right and left visual fields that takes place at the optic chiasm,[37] the coupling suggests that binocular growth is coordinated by processes that operate beyond the optic chiasm, a finding that has not been previously reported as far as we are aware. Alternatively the bilateral symmetry of retinal shape evident between temporal–nasal regions in the coronal plane (referenced to a vertical line midline drawn through the nose) could arise from growth orchestrated by diffusion gradients of signaling molecules.[38]

Since there were no significant differences between emmetropia and myopia with regard to maximum globe dimensions and globe dimensions at NP2 (i.e., dimensions orthogonal to the visual axis) for temporal to nasal quadrants and inferior to superior quadrants (Table 3), it is apparent that the differences in posterior vitreous chamber shapes indicated in Figures 4, 5, and 6 occur in the section of the chamber posterior to the respective points of maximum width (i.e., Fig. 7).

Based on the close match between actual and equivalent ellipse plots in Figure 7 and $a$ to $b$ ratio data in Table 3, posterior chamber shape in emmetropia can be categorized clearly as that of an oblate ellipse and in myopia as an oblate ellipse of a much lesser degree than emmetropia such that it approximates to a sphere, a finding that is consistent with that of a previous T1-weighted MRI study.[23]

Given the premise that the shape of the vitreous chamber is inherently elliptical in nature, the conic sections in Figure 8 illustrate schematically that the oblate ellipse that characterizes an emmetropic eye (semi-axis EY) will evolve geometrically to a less oblate ellipse with an increase in axial length. Thus with maximum globe widths (XYZ) not significantly different between refractive groups (Table 3), and VCD in emmetropia (YE) increasing (Table 3) to produce myopia (YM), a natural consequence will be for vitreous chamber shape to become less oblate and ultimately spherical, an outcome that is clearly evident in Figures 4, 5, and 6.

As prolate ellipse posterior chamber shapes were rarely found in the present study in subjects with myopia (Table 3), a supposition is that axial elongation is attenuated if the shape of postequatorial regions of the posterior chamber approaches that of a sphere; that is, a spherical shape may constitute a biomechanical limitation on further axial elongation in myopia. Prolate ellipse posterior chamber shapes, as defined in this study, may therefore only occur in eyes exhibiting very high degrees of myopia and associated pathological changes,[27–29] neither of which applied to the myopic group employed in the present study. A corollary of the supposition is that incipient
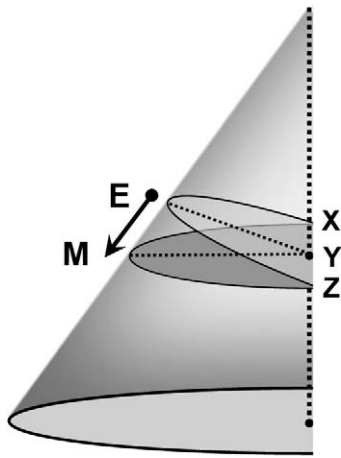
**Figure 8.** Semiconic sections to demonstrate schematically that an oblate ellipse of axis YE will become less oblate and ultimately spherical as axis length is increased to YM when axis XYZ remains constant.

it approximates to a sphere. Since prolate ellipse posterior chamber shapes were rarely found in the present study in subjects with myopia, we propose that spherical shape may constitute a biomechanical limitation on further axial elongation in myopia. The observation that the posterior chamber shape appears to be synchronized with retinotopic projection into visual fields suggests that binocular growth is coordinated by processes that operate beyond the optic chiasm.

myopia in eyes with posterior chamber shapes that are markedly oblate may be predisposed to more progression of myopia than those with less oblate shapes.

That emmetropia and myopia can be differentiated with reference to axial dimensions of the vitreous chamber but not equatorial dimensions (Figs. 4, 7) is of particular interest. Using chick eyes, Fischer et al.[39] showed that axial growth and equatorial growth can be independently modulated by the retina in a vision-dependent manner. They found that bullwhip and mini-bullwhip cells, like conventional glucagon-expressing amacrine cells, form part of retinal circuitry that detects image defocus to regulate precisely equatorial growth of the eye.[39] It has also been shown that axial growth of the vitreous chamber in chick eye is inhibited significantly when peripheral hyperopic retinal defocus is imposed across the central visual field by the wearing of two-zone negative lenses.[8] Owing to the presence of substantial image degradation it seems unlikely that the visual field at the equator is programmed to respond to defocus signals, and it is plausible therefore that axial and equatorial growth are independently regulated.

Mutti and colleagues[40,41] have proposed, however, that an enlarged ciliary muscle in the developing eye restricts equatorial expansion of the globe, resulting in an attenuation of crystalline lens thinning. The resulting loss in crystalline lens power consequently fails to compensate for the increasing axial length, and myopia ensues. However, evidence is equivocal that altered mechanical properties of the ciliary muscle can restrict the equatorial expansion needed to maintain emmetropia (Bailey M, et al. *IOVS* 2013;54:ARVO E-Abstract 5715).[42–44] With reference to data from the Singapore Cohort Study of the Risk Factors for Myopia (SCORM) study,[36] Iribarren et al.[45] have comprehensively analyzed longitudinal changes in lens thickness and power in children aged 6 to 9 years and consider that compaction in the lens nucleus can also account for lens thinning and a loss of internal power by a steepening of the gradient index.

The evidence implies therefore that the development of equatorial dimensions and crystalline lens properties are intrinsic and operate independently and that the ultimate refractive outcome is determined by the response of longitudinal axial growth to the nature of peripheral defocus[7] spanning the posterior pole.[46]

In summary, posterior vitreous chamber shape in emmetropia can be categorized as that of an oblate ellipse and in myopia as an oblate ellipse of significantly less degree such that

## References

1. Flitcroft, DI. The complex interactions of retinal, optical and environmental factors in myopia aetiology. *Prog Ret Eye Res*. 2012;31:622–660.

2. Flitcroft DI. Is myopia a failure of homeostasis? *Exp Eye Res*. 2013;114:16–24.

3. Wallman J, Winawer J. Homeostasis of eye growth and the question of myopia. *Neuron*. 2004;43:447–468.

4. Pan C-W, Ramamurthy D, Saw S-M. Worldwide prevalence and risk factors for myopia. *Ophthalmic Physiol Opt*. 2012;32:3–16.

5. Ganesan P, Wildsoet CF. Pharmaceutical intervention for myopia control. *Expert Rev Ophthalmol*. 2010;5:759–787.

6. Walline JJ, Lindsley K, Vedula SS, Cotter SA, Mutti DO, Twelker JD. Interventions to slow progression of myopia in children (Review). *Cochrane Database Syst Rev*. 2011;12CD004916.

7. Smith EL III. Prentice Award Lecture 2010: a case for peripheral optical treatment strategies for myopia. *Optom Vis Sci*. 2011;88:1029–1044.

8. Liu Y, Wildsoet C. The effective add inherent in 2-zone negative lenses inhibits eye growth in myopic young chicks. *Invest Ophthalmol Vis Sci*. 2012;53:5085–5093.

9. Sankaridurg P, Donovan L, Varnas S, et al. Spectacle lenses designed to reduce progression of myopia: 12 month results. *Optom Vis Sci*. 2010;87:631–641.

10. Sankaridurg P, Holden B, Smith EL III, et al. Decrease in rate of myopia progression with a contact lens designed to reduce relative peripheral hyperopia: one-year results. *Invest Ophthalmol Vis Sci*. 2011;52:9362–9367.

11. Anstice NS, Phillips JR. Effect of dual-focus soft contact lens wear on axial myopia progression in children. *Ophthalmology*. 2011;118:1152–1161.

12. Walline JJ, Jones LA, Sinnott L, et al. A randomized trial of the effect of soft contact lenses on myopia progression in children. *Invest Ophthalmol Vis Sci*. 2008;49:4702–4706.

13. Kakita T, Hiraoka T, Oshika T. Influence of overnight orthokeratology on axial elongation in childhood myopia. *Invest Ophthalmol Vis Sci*. 2011;52:2170–2174.

14. Hiraoka T, Kakita T, Okamoto F, Takahashi H, Oshika T. Long-term effect of overnight orthokeratology on axial length elongation in childhood myopia: a 5-year follow-up study. *Invest Ophthalmol Vis Sci*. 2012;53:3913–3919.

15. Santodomingo-Rubido J, Villa-Collar C, Gilmartin B, Gutierrez-Ortega R. Myopia control with orthokeratology contact lenses in Spain: refractive and biometric changes. *Invest Ophthalmol Vis Sci*. 2012;53:5060–5065.

Investigative Ophthalmology & Visual Science

16. Cho P, Cheung SW. Retardation of Myopia in Orthokeratology (ROMIO) study: a 2-year randomized clinical trial. *Invest Ophthalmol Vis Sci*. 2012;53:7077–7085.

17. Sng CC, Lin XY, Gazzard G, et al. Change in peripheral refraction over time in Singapore Chinese children. *Invest Ophthalmol Vis Sci*. 2011;52:7880–7887.

18. Mutti DO, Sinnott LT, Mitchell GL, et al. Relative peripheral refractive error and the risk of onset and progression of myopia in children. *Invest Ophthalmol Vis Sci*. 2011;52:199–205.

19. Smith EL III, Campbell MCW, Irving EL. Point-counterpoint. Does peripheral retinal input explain the promising myopia control effects of corneal reshaping therapy (CRT or ortho-K) & multifocal soft contact lenses? *Ophthalmic Physiol Opt*. 2013;33:379–384.

20. Berntsen DA, Barr CD, Mutti DO, Zadnik K. Peripheral defocus and myopia progression in myopic children randomly assigned to wear single vision and progressive addition lenses. *Invest Ophthalmol Vis Sci*. 2013;54:5761–5770.

21. Verkicharla PK, Mathur A, Mallen EAH, Pope JM, Atchison DA. Eye shape and retinal shape, and their relation to peripheral refraction. *Ophthal Physiol Opt*. 2012;32:184–189.

22. Atchison DA, Jones CE, Schmid KL. Eye shape in emmetropia and myopia. *Invest Ophthalmol Vis Sci*. 2004;45:3380–3386.

23. Atchison DA, Pritchard N, Schmid KL, Scott DH, Jones CE, Pope JM. Shape of the retinal surface in emmetropia and myopia. *Invest Ophthalmol Vis Sci*. 2005;46:2698–2707.

24. Singh KD, Logan NS, Gilmartin B. Three-dimensional modelling of the human eye based on magnetic resonance imaging. *Invest Ophthalmol Vis Sci*. 2006;47:2272–2279.

25. Ishii K, Iwata H, Oshika T. Quantitative evaluation of changes in eyeball shape in emmetropization and myopic changes based on elliptic Fourier descriptors. *Invest Ophthalmol Vis Sci*. 2011;52:8585–8591.

26. Lim LS, Yang X, Gazzard G, et al. Variations in eye volume, surface area, and shape with refractive error in young children by magnetic resonance imaging analysis. *Invest Ophthalmol Vis Sci*. 2011;52:8878–8883.

27. Moriyama M, Ohno-Matsui K, Hayashi K, et al. Topographic analyses of shape of eyes with pathologic myopia by high-resolution three dimensional magnetic resonance imaging. *Ophthalmology*. 2011;118:1626–1637.

28. Moriyama M, Ohno-Matsui K, Modegi T, et al. Quantitative analyses of high resolution 3D MR images of highly myopic eyes to determine their shapes. *Invest Ophthalmol Vis Sci*. 2012;53:4510–4518.

29. Ohno-Matsui K, Akiba M, Modegi T, et al. Association between shape of sclera and myopic retinochoroidal lesions in patients with pathologic myopia. *Invest Ophthalmol Vis Sci*. 2012;53:6046–6061.

30. Lim LS, Chong GH, Tang PT, et al. Distribution and determinants of eye size and shape in newborn children: a magnetic resonance imaging analysis. *Invest Ophthalmol Vis Sci*. 2013;54:4791–4797.

31. Davies LN, Mallen EAH, Wolffsohn JS, Gilmartin B. Clinical evaluation of the Shin-Nippon NVision-K 5001/Grand Seiko WR 5100K autorefractor. *Optom Vis Sci*. 2003;80:320–324.

32. Santodomingo-Rubido J, Mallen EAH, Gilmartin B, Wolffsohn JS. A new non-contact optical device for ocular biometry. *Br J Ophthalmol*. 2002;86:458–462.

33. Sheppard AL, Evans CJ, Singh KD, Wolffsohn JS, Dunne MCM, Davies LN. Three-dimensional magnetic resonance imaging of the phakic crystalline lens during accommodation. *Invest Ophthalmol Vis Sci*. 2011;52:3689–3697.

34. Armstrong RA, Davies LN, Dunne MCM, Gilmartin B. Statistical guidelines for clinical studies in human vision. *Ophthalmic Physiol Opt*. 2011;31:123–136.

35. Jones LA, Mitchell GL, Mutti DO, Hayes JR, Moeschberger ML, Zadnik K. Comparison of ocular component growth curves among refractive error groups in children. *Invest Ophthalmol Vis Sci*. 2005;46:2317–2327.

36. Wong H-B, Machin D, Tan S-B, Wong T-Y, Saw S-M. Ocular component growth curves among Singaporean children with different refractive error status. *Invest Ophthalmol Vis Sci*. 2010;51:1341–1347.

37. Bron AJ, Tripathi RC, Tripathi BJ. *Wolffe's Anatomy of the Eye and Orbit*. 8th ed. London: Chapman & Hall Medical; 1997: 535–587.

38. Wolpert L. Positional information and patterning revisited. *J Theor Biol*. 2011;269:359–365.

39. Fischer AJ, Ritchey ER, Scott MA, et al. Bullwhip neurons in the retina regulate the size and shape of the eye. *Dev Biol*. 2008;317:196–212.

40. Mutti DO. Hereditary and environmental contributions to emmetropization and myopia. *Optom Vis Sci*. 2010;87:255–259.

41. Mutti DO, Mitchell GL, Sinnott LT, et al.; CLEERE Study Group. Corneal and crystalline lens dimensions before and after myopia onset. *Optom Vis Sci*. 2012;89:251–262.

42. Buckhurst H, Gilmartin B, Cubbidge RP, Nagra M, Logan NS. Ocular biometric correlates of ciliary muscle thickness in human myopia. *Ophthal Physiol Opt*. 2013;33:294–304.

43. Ishii K, Yamanari M, Yasuno Y, Oshika T. Relationship between changes in crystalline lens shape and axial elongation in young children. *Invest Ophthalmol Vis Sci*. 2013;54:771–777.

44. Pucker AD, Sinnott LT, Kao C-Y, Bailey MD. Region-specific relationships between refractive error and ciliary muscle thickness in children. *Invest Ophthalmol Vis Sci*. 2013;54: 4710–4716.

45. Iribarren R, Morgan IG, Chan YH, Lin X, Saw S-M. Changes in lens power in Singapore Chinese children during refractive development. *Invest Ophthalmol Vis Sci*. 2012;53:5124–5130.

46. Mathur A, Atchison DA. Peripheral refraction patterns out to large field angles. *Optom Vis Sci*. 2013;90:140–147.